Carbothermic Reduction of Stainless Steel Dust for Producing Fine Spherical Metallic Powders

Lichun Zheng[1,2], Annelies Malfliet[2], Huabing Li[1], Zhouhua Jiang[1], Bart Blanpain[2], Muxing Guo[2]

1. School of Metallurgy, Northeastern University, Wenhua Road 3-11, Heping District, Shenyang 110819, China
2. Department of Materials Engineering, KU Leuven, Kasteelpark Arenberg 44 box 2450, Leuven 3001, Belgium

In this work, we explored the possibility of producing fine spherical metallic powders via carbothermic reduction of stainless steel dust. For this purpose, stainless steel dust was reduced with carbon using a vertical tube furnace in the temperature range of 1000–1300 °C, focusing on the characteristics of the obtained metallic particles. High temperature and long reduction time favour stainless steel dust reduction. The reduction was almost completed during the first 10 min at 1300 °C. The metallic particles obtained at 1000 °C and 1200 °C are very irregular. At 1300 °C, however, more than half (>55.0%) of the metallic particles become spherical or near-spherical (aspect ratio < 1.5), especially when extending the reduction time to 30 min. The irregular metallic particles generated at 1300 °C are attributed to the presence of M_7C_3 carbide in the particles. Metallic particle growth accelerates considerably with reduction time. The two-step reduction method, i.e., reducing SSD at 1000 °C for 30 min and re-reducing it at 1300 °C for 10 min, facilitates the formation of fine and near-spherical metallic particles. Factors influencing the characteristics of the metallic particles are discussed.

1. Introduction

Stainless steel dust (SSD) is generated during s45tainless steel production due to ejection of metal and slag droplets by bursting of bubbles on the bath surface(Delhaes et al., 1993), and collected at off-gas cleaning system. Approximately, 20 kg SSD per ton of crude steel is formed in the EAF (Electric Arc Furnace) process(Best and Pickles, 2001; Sofilić et al., 2004) and 10 kg in the AOD (Argon Oxygen Decarburization) process(Delhaes et al., 1993). The SSD contains significant amounts of valuable metals, such as Zn, Cr, Fe and Ni, in the form of complex oxides(Delhaes et al., 1993; Laforest and Duchesne, 2006; Ri and Chu, 2015; Yang et al., 2019). However, SSD has been classified as hazardous waste in many countries as Pb, Cd and hexavalent Cr contained in SSD can be leached into ground water at unacceptable levels under naturally occurring conditions(Laforest and Duchesne, 2006; Ma and Garbers-Craig, 2006).

To reduce the harmful effects of SSD on environment, SSD has to be treated sufficiently before final

disposal. The treatment of SSD has been an important research topic and a number of methods have been developed over several decades. These treatment methods can be divided into two categories: (1) Stabilizing SSD with some additives(Cholake et al., 2018; Lozano-Lunar et al., 2019; Mymrin et al., 2016; Sayadi and Hesami, 2017). This method converts chemically unstable SSD into stable products, which are either landfilled or used as cement, glass, ceramic, etc. The valuable metals in SSD are not recovered. Moreover, very long-term stability (over tens of years) of these products has not been confirmed experimentally yet(Pereira et al., 2007); (2) Recovering the metals via solid-state reduction or smelting reduction processes for recycling or reutilization in stainless steel production(De Araújo and Schalch, 2014; Görnerup and Lahiri, 1998; Hanewald and Dombrowski, 1985; Hara et al., 2000; Hasegawa et al., 1998; Ichikawa and Morishige, 2003; Lemperle et al., 2011; Ri et al., 2016; Takano et al., 2005). This method uses carbonaceous materials, ferrosilicon or aluminum to reduce SSD at high temperatures for recovering Zn, Cr, Fe and Ni. Solid-state reduction processes, such as DryIron(Ichikawa and Morishige, 2003) and INMETCO(Hanewald and Dombrowski, 1985), have low recovery rates of Cr, Fe and Ni due to relatively low temperatures, leading to a large amount of valuable metals lost in the residue. Smelting reduction processes, such as STAR(Hasegawa et al., 1998) and OxyCup(Lemperle et al., 2011) have the advantages of almost complete recovery of the valuable metals and sufficient slag-metal separation at very high temperatures. However, these processes are less economical due to high energy consumption. Currently, a large fraction of SSD is not treated sufficiently to recover the valuable metals(Nakayama, 2012; Ye et al., 2003), because of large capital investment in processing facilities together with the relatively low value of the reduced metals, compared with the total processing cost. Fine stainless steel powders, especially of spherical morphology, have a substantially higher value than its bulk material(Walther et al., 2015; Yolton and Froes, 2015). Therefore, to maximize the value of the obtained metallic products, we propose in this paper a new concept to produce fine spherical metallic powders via carbothermic reduction of SSD. The obtained fine spherical metallic powders could be used for powder metallurgy techniques or 3D-printing, depending on metallic particle characteristics regarding size, roundness and impurity level.

Thermal reduction of oxides is a very traditional and predominant method of producing metallic powders(Finlayson and Morrell, 1968; Ramakrishnan, 1983). This process utilizes solid or gaseous reducing agents, such as carbon and hydrogen, to reduce pure oxides or oxide mixtures. Both pure metal powders and alloy powders, such as iron(Benchiheub et al., 2010; Martín et al., 2012, 2010; Ramakrishnan, 1983; Walther et al., 2015), Co-W(Lebukhova and Karpovich, 2006), Ni-Mo(Lebukhova and Karpovich, 2008) and V-Ti(Suzuki et al., 2004), can be produced via this method. The reduction temperature is usually controlled far below the melting point of the metallic powders to suppress their sintering. Even though, severe sintering of the metallic powders is inevitable as they are in close contact with each other at high temperatures. Moreover, the reduced metallic powders have irregular morphologies as they are in solid state during reduction.

Theoretically, these two issues can be avoided when using SSD as raw material to produce metallic powders via carbothermic reduction, thanks to the following two reasons: (1) A certain amount of carbon dissolved into metallic powders during reduction can significantly lower the melting point of the metallic powders. Taking Fe-20%Cr alloy as an example, addition of 3.0% carbon dramatically decreases its melting point from 1496 °C to 1278 °C(Kavulicova et al., 2006). Within a proper temperature range of reduction, the reduced metallic powders are in liquid state while the surrounding residual oxides are in solid state. The metallic droplets have poor wettability on the oxides(Kozakevi.P and Olette, 1971; Nogi and Ogino, 1983), exhibiting a near-spherical morphology under the imposed surface tension. (2) The presence of solid residual oxides among metallic droplets can hinder the rapid growth of the metallic droplets, favouring the production of fine metallic powders. Currently, carbothermic reduction of SSD and other metallurgical wastes have been extensively studied. Fine and near-spherical metallic particles were observed under certain conditions(Huang et al., 2011; Liu et al., 2017; Ri and Chu, 2015; Tsuji, 2012; Xia et al., 2015). However, optimal conditions and mechanisms for forming fine spherical metallic particles from SSD have not been reported yet.

In this paper we explore the possibility of producing fine spherical metallic powders via carbothermic reduction of SSD at relatively low temperatures. For this purpose, fine SSD together with carbon powders was reduced under various conditions. The reduced metallic particles were analysed in terms of chemical composition, size distribution and morphology. Factors influencing the size and morphology of the reduced metallic particles are discussed.

2. Experimental

2.1. Material

The SSD used in this work was provided by Orbix company, Belgium. Table 1 shows the chemical composition of the SSD analysed with wavelength dispersive X-ray fluorescence (WD-XRF) spectrometers (Philips PW 2400). Figure 1 shows the microstructure of the SSD analysed with an electron probe micro-analyser (FEG-EPMA JXA-8530F), equipped with wavelength dispersive spectrometers (WDS). The chemical compositions of the main phases observed in the SSD are presented in Table 2. Phase A is occasionally observed metallic particles. Oxide phases B and C contain several percent of Fe but no Cr. Phase D is an almost pure Fe-Cr-O oxide. The matrix phase E contains 50.15% Fe_2O_3 and 19.17%Cr_2O_3. Obviously, majorities of Fe and Cr exist in the matrix phase. Before carbothermic reduction, the SSD was dried in a muffle furnace at 300 °C for 2 hours.

Table 1 The chemical composition of the SSD, expressed as wt.% oxides and normalized.

Fe_2O_3	Cr_2O_3	ZnO	NiO	MnO	SiO_2	CaO	MgO	PbO	MoO_3	P_2O_5
45.00	13.62	7.37	0.10	1.20	3.53	20.45	8.21	0.11	0.13	0.27

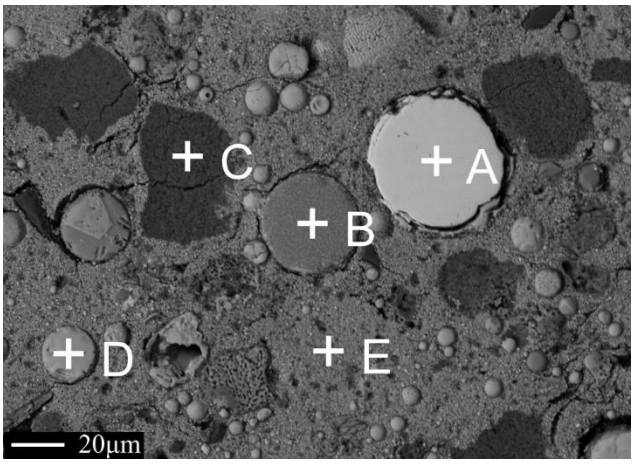

Fig. 1 Microstructure of the SSD.

Table 2 The chemical compositions of the phases observed in SSD, wt.%.

Phase No.	Fe	Cr	Si			
A	92.8	6.9	0.3			
	Fe_2O_3	Cr_2O_3	SiO_2	CaO	MgO	ZnO
B	8.1	-	1.9	81.7	2.1	6.1
C	3.4	-	-	41.2	55.4	-
D	74.7	23.7	-	1.1	0.5	-
E	50.2	19.2	6.2	9.9	2.2	12.3

2.2. Procedure

Carbothermic reduction of the SSD was conducted in a $MoSi_2$ resistance-heated vertical tube furnace (80 mm ID, 1000 mm H) in a flowing argon atmosphere. The SSD and reductant carbon were ground separately to pass a 74-μm sieve. 5 grams of the SSD and 0.77 gram of carbon powders were well mixed and filled into a MgO crucible (27 mm ID, 50 mm H). The atomic ratio of carbon to oxygen contained in the reducible oxides, i.e., Fe_2O_3, Cr_2O_3, ZnO, MnO, NiO, and MoO_3, is 1.07, with the purpose of dissolving a certain quantity of carbon into the metallic product to lower its liquidus temperature. The furnace was first heated to a prescribed temperature under air and held there for 30 min. Afterwards, the MgO crucible, hanged by a Pt wire, was put into the furnace in a low temperature zone (< 100 °C), which is approximately 10 cm away from the top of the furnace. The furnace tube was purged with high purity argon gas at a flow rate of 5 $L \cdot min^{-1}$ for 10 min to remove impurities. Thereafter, argon flow rate was decreased to 0.3 $L \cdot min^{-1}$. Then, the MgO crucible was rapidly lowered to the centre of the furnace for isothermal reduction. After a pre-set time, the MgO crucible was rapidly taken out of the furnace and quenched in a stream of argon gas. The experimental conditions are listed in Table 3.

Table 3 Details of the experimental conditions.

Test No.	Temperature (°C)	Reduction time (min)

T1	1000	30
T2	1200	30
T3	1300	10
T4	1300	30
T5	1000 + 1300	30 + 10

Note: For test T5, the sample was first reduced at 1000 °C for 30 min and then further re-reduced at 1300 °C for 10 min.

2.3. Characterization

Before and after carbothermic reduction, each sample was carefully weighted using a weighing scale accurate to 0.0001 g. Thereafter, the samples were crushed into small pieces. For each sample, several pieces were mounted in epoxy resin, ground, polished and finally coated with Pt-Au. Post-test examination of the samples was performed with the above mentioned EPMA operated at 15 kV voltage and 30 nA current. To measure the size of the reduced metallic particles, successive micrographs were taken using the EPMA in backscattered electron (BSE) mode. The micrographs were processed with an image analyser to measure the size of the metallic particles. The size of a single metallic particle is described by its equivalent diameter, which is defined as the diameter of a circle with the same area as the particle. More than 1400 metallic particles larger than 2 μm were counted in.

3. Experimental results

3.1. Weight loss

To characterize the extent of carbothermic reduction of the SSD, the weight loss of the SSD and carbon mixture under various conditions is presented in Figure 2. The theoretical maximum weight loss, which was calculated by assuming that all oxygen contained in Fe_2O_3, Cr_2O_3, ZnO, MnO, SiO_2, NiO, PbO, MoO_3 oxides reacts with carbon to form CO gas and that the reduced Zn metal volatilizes completely, is also given in the figure. The measured weight losses of the samples reduced at 1000 °C, 1200 °C and 1300 °C for 30 min are 21.3%, 30.6% and 33.4%, respectively, indicating that a high temperature favours the reduction of the SSD. This is consistent with previous reports(Long et al., 2012; Tang et al., 2018; Yoshikawa et al., 2008). Note that for the sample reduced at 1300 °C for 30 min the weight loss (33.4%) is quite close to the theoretical maximum value (35.2%). Moreover, at 1300 °C, the weight loss only increases by 2.1% when extending the reduction time from 10 min to 30 min, suggesting that carbothermic reduction of the SSD at 1300 °C was almost completed during the first 10 min. The sample reduced at 1000 °C for 30 min and then re-reduced at 1300 °C for 10 min (two-step reduction) has a weight loss of 33.8%, which is 2.5% higher than the sample only reduced at 1300 °C for 10 min.

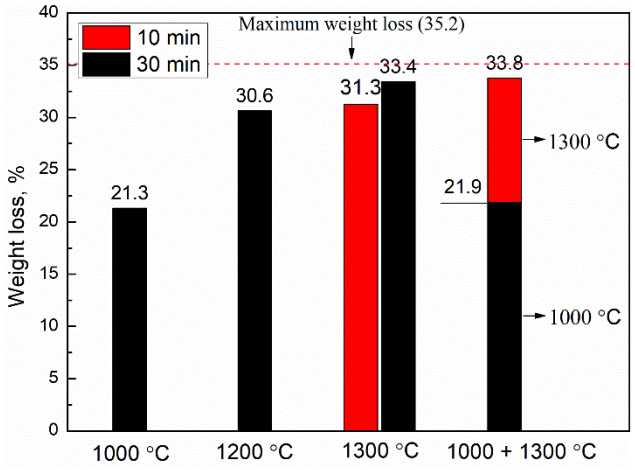

Fig. 2 Weight loss of the SSD after carbothermic reduction at various conditions.

3.2. Morphology of the metallic particles

Figure 3 gives an overview of the metallic particles on the polished cross-sections under various conditions. The metallic particles reduced at 1000 °C and 1200 °C are very irregular in morphology (Figs. 3a and 3b). Besides numerous small bead-like metallic particles, both large finger-like and dendritic metallic particles were frequently observed. A similar phenomenon was also reported by Zhang et al(Zhang et al., 2014). At 1300 °C, however, no dendritic metallic particles were observed. Finger-like metallic particles were only occasionally observed in the sample reduced for a short time, i.e., 10 min (Figs. 3c and 3d). When extending the reduction time from 10 min to 30 min, more particles have a rounded morphology, especially the small particles (Figs. 3e and 3f). Therefore, it can be concluded that high temperature and long reduction time favour the formation of spherical particles. For the two-step reduction sample, large finger-like metallic particles were more frequently observed (Figs. 3g and 3h), compared with the samples only reduced at 1300 °C for 10 min (Figs. 3c and 3d). Dendritic metallic particles were rarely found in the two-step reduction sample.

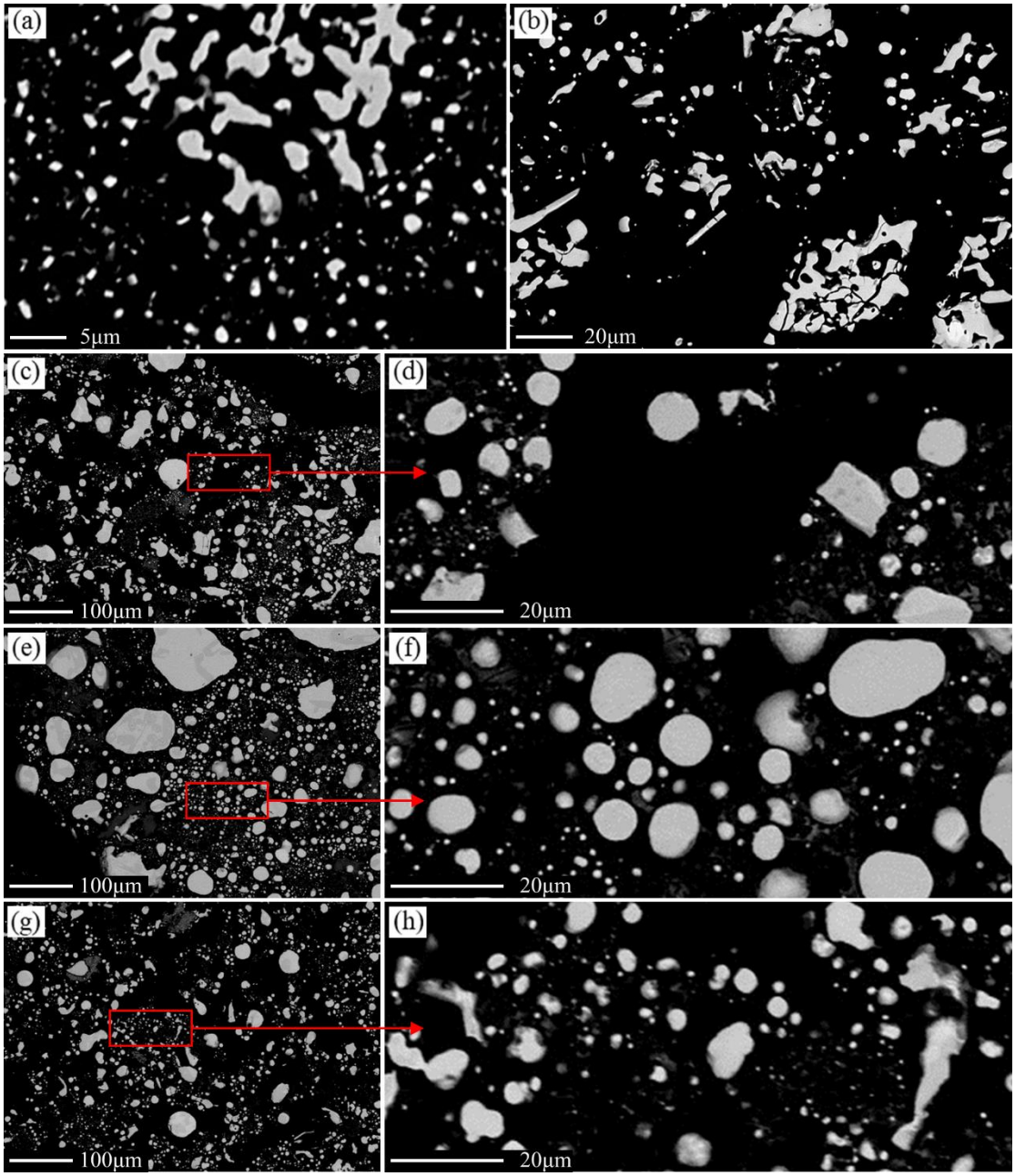

Fig. 3 Morphology of metallic particles after carbothermic reduction under various conditions. (a) T1: 1000 °C and 30 min; (b) T2: 1200 °C and 30 min; (c) and (d) T3: 1300 °C and 10 min; (e) and (f) T4: 1300 °C and 30 min; (g) and (h) T5: two-step reduction.

To quantitatively characterize the morphology of the metallic particles, the mean aspect ratio of the metallic particles as a function of particle size is plotted in Figure 4. The aspect ratio of a particle is defined as the ratio of the long and short axis of the Legendre ellipse equivalent to the particle(Mikli et al., 2001). For the sample reduced at 1300 °C for 10 min, the mean aspect ratio roughly increases with increasing particle size. This result is consistent with the observation in Figs. 3c and 3d. For the sample reduced at 1300 °C for 30 min, there is no clear trend of the particle aspect ratio versus particle size. The average mean aspect ratio of the metallic particles is smaller than the short-time

sample (10 min) for all size ranges, where the mean aspect ratios are below 1.55. The two-step reduction sample shows a similar trend as the sample reduced at 1300 °C for 10 min.

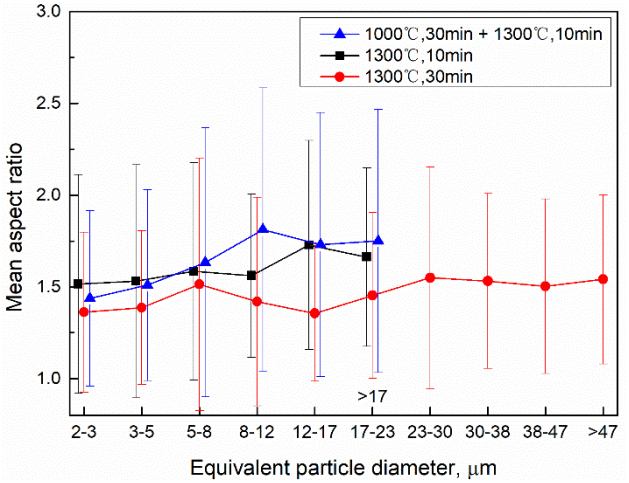

Fig. 4 Mean aspect ratio of the metallic particles versus particle size under various conditions. The bars represent the standard deviation of the measured aspect ratio.

Figure 5 shows the cumulative area versus aspect ratio of the metallic particles for the above three samples. The sample reduced at 1300 °C for 30 min has the highest cumulative area at a given aspect ratio (excluding 1.2) among the three samples. Taking the particles with an aspect ratio below 1.5 as an example, the area fraction of such particles in the sample reduced at 1300 °C for 30 min is 65 %, whereas it is 55 % in the sample reduced at 1300 °C for 10 min and 61 % in the two-step reduction sample. Compared with the sample reduced at 1300 °C for 10 min, the two-step reduction method generates relatively more near-spherical particles with aspect ratio below 1.5. Note that irregular particles with aspect ratio over 2.1 also become more in the two-step reduction sample. Thus, it can be concluded that the two-step reduction method helps in producing near-spherical metallic particles (aspect ratio < 1.5).

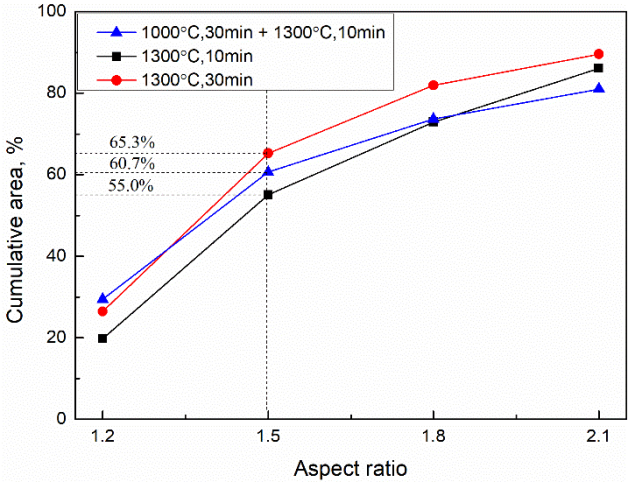

Fig. 5 Cumulative area versus aspect ratio of the metallic particles.

3.3. Size distribution of the metallic particles

Figure 6 shows the area-based cumulative size distribution of the metallic particles. Clearly, the sample reduced at 1300 °C for 10 min has much smaller size than the sample reduced at the same temperature for 30 min. Taking the particles below 20 μm as an example, extending the reduction time from 10 min to 30 min, the percentage decreases sharply from 60.4% to 36.6%, indicating that the metallic particles grow up rapidly with time. Compared with the sample only reduced at 1300 °C for 10 min, a much smaller particle size was obtained in the two-step reduction sample, where up to 74.2% particles are below 20 μm. Therefore, by shortening the reduction time and adopting a two-step reduction method the metallic particle size can be significantly decreased.

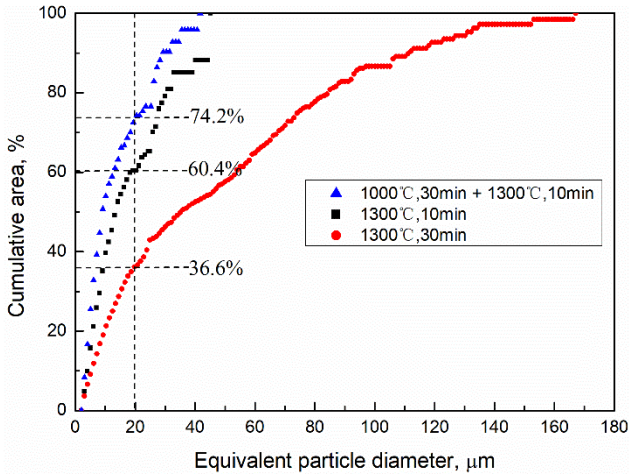

Fig. 6 Cumulative size distribution of the metallic particles.

3.4. Microstructural and compositional analysis

Figure 7a shows the microstructure of the particles in the sample reduced at 1300 °C for 30 min. In the BSE images, two different phases, i.e., a light grey phase and dark grey phase (indicated by red arrows), were observed in the particles. The dark grey phase was found in almost all irregular particles in both samples. In the near-spherical particles, however, the dark grey phase was only occasionally identified. Compositional analysis given in Table 4 reveals that the dark grey phase is $(Fe,Cr,Mn)_7C_3$ carbide (denoted as M_7C_3), which is consistent with a previous report (Lindblom, 2005). The M_7C_3 carbides are in bar- and/or plate-like shapes, which was also observed by previous studies(Bedolla-Jacuinde et al., 2005; Wu et al., 2007). The light grey phase has lower C and Cr contents compared with the dark grey phase. Figure 7b is an enlarged view of the light grey phase, showing a eutectic structure. Possibly, the M_7C_3 carbide already exists at 1300 °C. Therefore, it may be concluded that presence of M_7C_3 carbide makes the particles irregular.

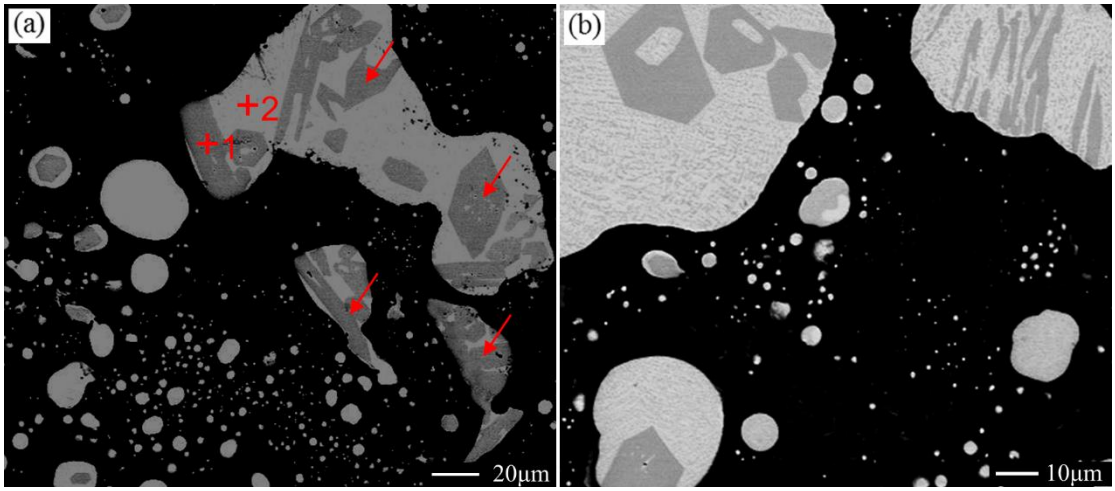

Fig. 7 Microstructure of the particles in the sample reduced at 1300 °C for 30 min. (a) low magnification; (b) high magnification.

Table 4 The chemical composition of the phases in the particles indicated in Fig. 7a, wt.%.

Point No.	Fe	Cr	Mn	Ni	Si	Zn	C	Note
1	62.9	23.7	4.5	0.1	0	0.1	8.8	$(Fe,Cr,Mn)_7C_{3.1}$
2	85.9	6.8	1.4	0.2	1.3	0.1	4.3	Eutectic mixture

Figure 8 shows the elemental mappings for both the reduced particles and residual oxides in the samples reduced at 1300°C for 30 min. The Fe and Cr distributions are inhomogeneous in the large reduced particles due to the M_7C_3 carbide formation. For the small particles, the core is Fe-rich, whereas the rim is enriched in Cr. The element distribution in the residual oxides is inhomogeneous. The residual oxides around the large reduced particles, as indicated by the dashed line in the BSE image, are rich in Ca and Si. The chemical composition analysis given in Table 5 together with the $CaO\text{-}SiO_2$ phase diagram (Eriksson et al., 1994) indicates that the residual oxides are mainly a mixture of Ca_2SiO_4 and CaO. On the contrary, Ca and Mg are predominant in the residual oxides around the small metallic particles located in the lower half of the BSE image. Based on the composition analysis in Table 5 and the CaO-MgO phase diagram (Wu et al., 1993), the residual oxides are mainly a mixture of CaO and MgO.

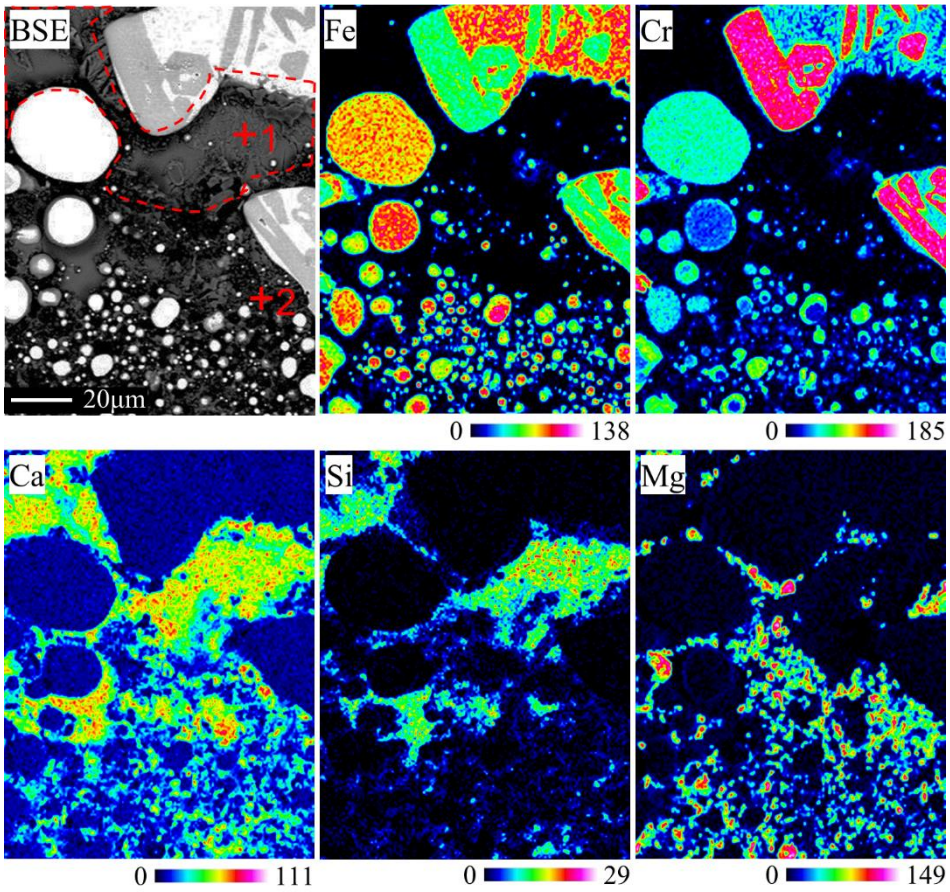

Fig. 8 Elemental mappings in the sample reduced at 1300 °C for 30 min.

Table 5 The chemical compositions of the residual oxides indicated in Fig. 8, wt.%.

Point No.	SiO_2	CaO	Al_2O_3	MgO	ZnO	SO_3	P_2O_5	FeO	Cr_2O_3	Note
1	26.8	68.4	1.1	0.5	0.02	0.4	0.8	1.1	0.8	Ca_2SiO_4+CaO
2	2.1	29.5	0.3	63.2	0.05	3.3	0.3	0.4	0.9	CaO+MgO

3.5 Thermodynamic analysis

For a deeper understanding of the experimental observations and results, the carbothermic reduction of the SSD was calculated with the thermodynamic software FactSage 7.2 using the FSstel, FToxid and FactPS databases under the current experimental conditions.

Figure 9 shows the change in Cr and C content in the non-oxide reduction product as a function of temperature. Other solute elements, such as Si and Mn, are not shown in the figure due to their very low levels. Moreover, only the non-oxide reduction products are presented in this figure. The reduction product varies with temperature. At temperatures below 1055.5 °C, FCC iron containing approximately 1.5 wt.% C and trace amounts of Cr, Mn and other elements is formed. At temperatures between 1055.5 °C and 1187.6 °C, $(Fe,Cr,Mn)_3C$ carbide (denoted as M_3C) becomes thermodynamically stable instead of FCC iron. The C content in the M_3C carbide is around 6.7 wt.%, while the Cr content increases from 1.5 wt.% to 11.6 wt.% with increasing temperature. In the

temperature range of 1187.6– 1289.3 °C, two phases, i.e., $(Fe,Cr,Mn)_7C_3$ carbide (M_7C_3) and liquid metal, co-exist. The Cr content in the two phases increases linearly with temperature. More than 40 wt.% Cr is concentrated in the M_7C_3 phase. The C content in the liquid metal is around 4.6 wt.%. By further increasing the temperature, the M_7C_3 carbide dissolves completely into the liquid metal, forming a single liquid metallic phase with a composition of Fe-16.9%Cr-4.4%C-1.1%Mn at 1300 °C.

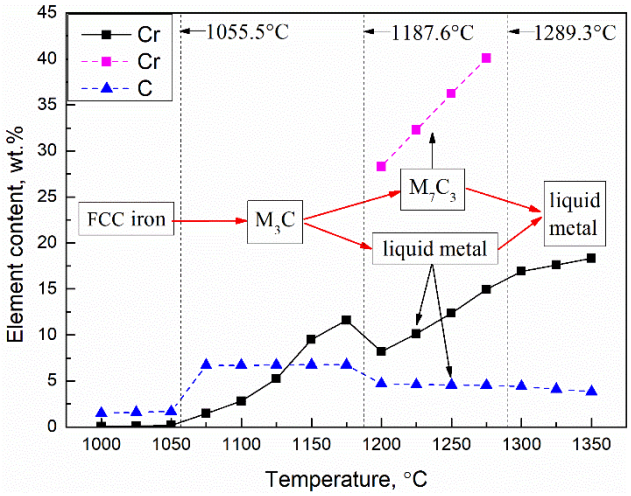

Fig. 9 Cr and C contents in reduction products versus temperature.

Figure 10 shows the reduction degree of Fe, Zn, Cr and Mn versus temperature. The reduction degree is defined as the ratio of the total amount of an element in non-oxide products after reduction to the total amount of the element in the SSD before reduction. The reduction degrees of Fe and Zn are close to 100% in the present investigated temperature range. Almost all Zn goes into the gas phase due to its low boiling point of 908 °C (Perry, 2011). This is the reason why the Zn content is extremely low in the metallic particles (Table 4). The Cr reduction degree becomes significant above 1075 °C and rises rapidly until 1200 °C. Then, it increases relatively slowly with further temperature increase. This explains why the weight loss of the samples increases significantly from 1000 °C to 1200 °C, while only slightly from 1200 °C to 1300 °C (Fig. 2). Note that the calculated reduction degree of Cr is only 73.5% even at 1300 °C. Mn reduction follows a similar behaviour to Cr but its reduction degree becomes lower than Cr for temperatures above 1150 °C.

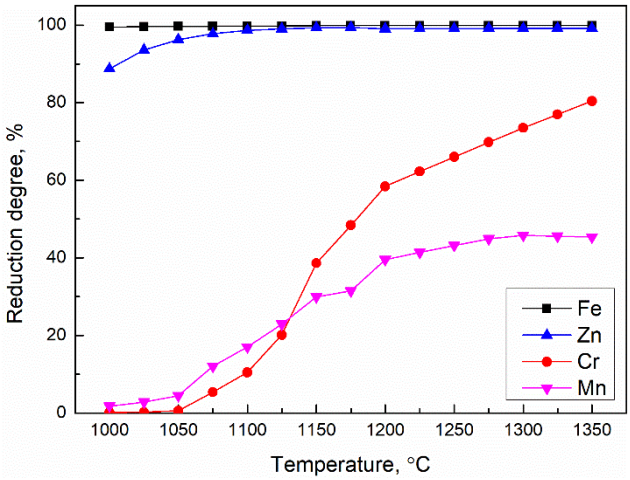

Fig. 10 Thermodynamically calculated reduction degree of reducible oxides as a function of temperature.

4. Discussion

In this work, both near-spherical and irregularly shaped reduced particles were obtained in the samples reduced at 1300 °C. Most irregular particles have a metallic matrix containing M_7C_3 carbides (Fig. 7). Thus, the distinct morphologies may be caused by different C and Cr contents in the metallic particles, which significantly affect M_7C_3 carbide precipitation at 1300 °C. Figure 11 shows the effect of C and Cr contents on the liquidus temperature of Fe-Cr-C alloys. The average Fe/Cr mass ratio in the SSD is 3.4. Considering the incomplete reduction of Cr oxides, the average Fe/Cr ratio in the metallic particles is higher. Taking $wt_{Fe}/wt_{Cr}=4$ as an example, metallic particles with C content in the range of 3.15–4.3 wt.% are in the liquid state at 1300 °C, without M_7C_3 carbide precipitation. These metallic particles should be near-spherical under the imposed surface tension. For particles with a C content above 4.3 wt.%, the liquidus temperature exceeds 1300 °C, leading to M_7C_3 carbide precipitation at 1300 °C. The formation of these blocky M_7C_3 precipitates may cause the reduced particles to have an irregular shape. For $wt_{Fe}/wt_{Cr}=3$, the critical C content for M_7C_3 carbide precipitation at 1300 °C decreases to 3.7%, greatly increasing the formation tendency of irregular metallic particles. The inhomogeneous SSD composition (Fig. 1) and carbon distribution in the samples are very likely to cause relatively high C and Cr contents in some metallic particles. Therefore, strictly controlling carbon addition and using finer raw materials may increase the relative amount of near-spherical metallic particles.

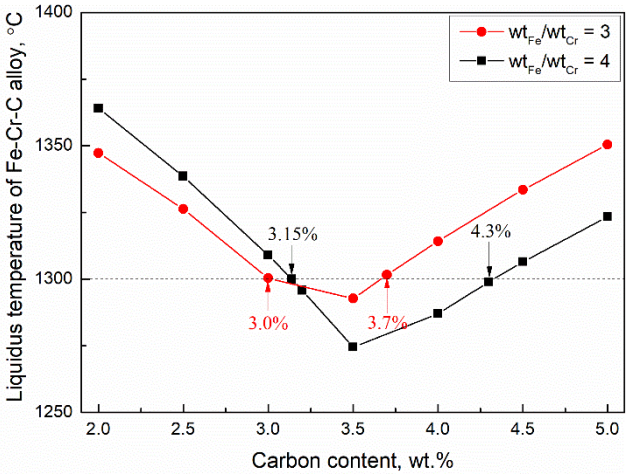

Fig. 11 Calculated liquidus temperature of Fe-Cr-C alloy versus C content with FactSage 7.2 using FSstel and FactPS databases.

The reduced particles grow rapidly at 1300 °C when extending the reduction time from 10 min to 30 min (Fig. 6). The slight increase of weight loss from 10 min to 30 min (Fig. 2) as well as the minor amounts of residual reducible oxides (Table 5) exclude the possibility that the rapid growth of metallic particles is attributed to further reduction of reducible oxides. Therefore, it can be speculated that the rapid growth might be due to the Ostwald ripening, i.e., a growth process of particles by the dissolution of coexisting smaller particles (Voorhees, 1985), and/or direct particle collisions. The latter could be ruled out as liquid slags have disappeared after 10 min at 1300 °C due to rapid consumption of iron oxides (Table 5 and Fig. 10). Particle growth by Ostwald ripening is controlled by the diffusion of growth materials in the neighbouring phase. As mentioned in section 3.4, large metallic particles are surrounded by CaO-SiO_2 oxides while small particles by CaO-MgO oxides. Therefore, it might be inferred that mass transfer through CaO-SiO_2 oxides is significantly faster than through CaO-MgO oxides. The exact reason is unknown currently. Possibly, the phenomenon that CaO-SiO_2 oxides are quite dense while CaO-MgO oxides are porous (Fig. 8) may account for the difference. Therefore, it might be inferred that the presence of SiO_2 promotes metallic particle growth by Ostwald ripening.

As seen in sections 3.2 and 3.3 (Figs. 3 and 6), the reduced particles obtained via the two-step reduction process (T5) have a smaller size than via the one step reduction (T3). This can be interpreted through the FeO-CaO-SiO_2 phase diagram (Zhang et al., 2006), according to which liquid slag could be formed at 1300 °C before substantial consumption of iron oxides for the one-step reduction samples. Liquid slag favours the growth of metallic particles. In the two-step reduction sample, however, liquid slag could not be formed as almost all of the iron oxides had been reduced at 1000 °C (Fig. 10). This results in a worse kinetics for metallic particle growth in the two-step reduction process. Moreover, the two-step reduction method not only generates relatively more near-spherical metallic particles (aspect ratio < 1.5), but also more irregular particles (aspect

ratio >2.1), compared with the one step reduction (Fig. 5). The following reasons may account for this phenomenon: (1) More small metallic particles (Fig. 6), which have smaller aspect ratio than large particles (Fig. 4), were formed via the two-step reduction method. Thus, the relative amount of near-spherical metallic particles increases; (2) Due to much longer reduction time in the two-step reduction sample, more carbon could be dissolved into the metallic particles and more Cr could be reduced, facilitating the formation of M_7C_3 carbides (Table 4). Consequently, the metallic particles containing M_7C_3 carbides becomes relatively more. These metallic particles naturally have irregular morphologies.

In summary, although high temperatures and long reduction times (Figs. 2 and 10) favour the formation of near-spherical metallic particles, it goes against the formation of fine metallic particles (Fig. 6). Therefore, these parameters should be closely controlled. The two-step reduction method facilitates the formation of fine and near-spherical metallic particles. This works demonstrates the possibility of producing fine spherical stainless steel powders via carbothermic reduction of SSD. Still, further work is necessary to improve the quality of the metallic particles. Also, decarburization and separation methods need to be developed to produce satisfactory stainless steel powders.

5. Conclusions

Carbothermic reduction of SSD in the temperature range of 1000–1300 °C was investigated. The results obtained are as follows:

1. High temperature and long reduction time favour SSD reduction. Especially at 1300 °C, the reduction was almost completed during the first 10 min.
2. The metallic particles reduced at 1000 °C and 1200 °C are irregular. At 1300 °C, however, more than half of the metallic particles become spherical or near-spherical, especially when extending the reduction time to 30 min. The irregular metallic particles appeared at 1300 °C are attributed to the presence of M_7C_3 carbide in the particles.
3. The metallic particles grow rapidly at 1300 °C when extending the reduction time from 10 min to 30 min. The two-step reduction method decreases the size of the metallic particles and increases the relative amount of near-spherical metallic particles.
4. SiO_2 in the residual oxides promotes the growth of the metallic particles, while MgO hinders the growth of the particles.

Acknowledgement

This work was supported by the Fundamental Research Funds for the Central Universities, NEU (N2025039). The authors thank the Orbix company in Belgium for financial support and for providing SSD.

References

Bedolla-Jacuinde, A., Hernández, B., Béjar-Gómez, L., 2005. SEM study on the M7C3 carbide nucleation during eutectic solidification of high-chromium white irons. Zeitschrift für Met. 96, 1380–1385.

Benchiheub, O., Mechachti, S., Serrai, S., Khalifa, M.G., 2010. Elaboration of iron powder from mill scale. J. Mater. Environ. Sci. 1, 267–276.

Best, T.E., Pickles, C.A., 2001. In-flight plasma reduction of electric arc furnace dust in carbon monoxide. Can. Metall. Q. 40, 61–78.

Cholake, S.T., Farzana, R., Numata, T., Sahajwalla, V., 2018. Transforming electric arc furnace waste into value added building products. J. Clean. Prod. 171, 1128–1139.

De Araújo, J.A., Schalch, V., 2014. Recycling of electric arc furnace (EAF) dust for use in steel making process. J. Mater. Res. Technol. 3, 274–279.

Delhaes, C., Hauck, A., Neuschutz, D., 1993. Mechanisms of dust generation in a stainless steelmaking converter. Steel Res. 64, 22–27.

Eriksson, G., Wu, P., Blander, M., Pelton, A.D., 1994. Critical evaluation and optimization of the thermodynamic properties and phase diagrams of the MnO–SiO2 and CaO–SiO2 systems. Can. Metall. Q. 33, 13–21.

Finlayson, P.C., Morrell, A.P., 1968. The peace river process for the production of iron powder. Powder Metall. 11, 224–232.

Görnerup, M., Lahiri, A.K., 1998. Reduction of electric arc furnace slags in stainless steelmaking Part 1 Observations. Ironmak. Steelmak. 25, 317–322.

Hanewald, R.H., Dombrowski, D.E., 1985. Recovery of metals from steel wastes and production of DRI by the INMETCO process. Iron Steel Eng. 62, 62–67.

Hara, Y., Ishiwata, N., Itaya, H., Matsumoto, T., 2000. Smelting reduction process with a coke packed bed for steelmaking dust recycling. ISIJ Int. 40, 231–237.

Hasegawa, S., Kokubu, H., Hara, Y., 1998. Development of a smelting reduction process for recycling steelmaking dust. KAWASAKI STEEL Tech. REPORT-ENGLISH Ed. 32–37.

Huang, D., Zhang, J., Mao, R., Cao, M., 2011. Thermal behaviors and growth of reduced ferronickel particles in carbon-laterite composites. Rare Met. 30, 681–687.

Ichikawa, H., Morishige, H., 2003. Rotary hearth furnace process for steel mill waste recycling and direct reduced iron making. Rev. Métallurgie 100, 349–354.

Kavulicova, J., Ivánová, D., Durisin, J., Sucik, G., Skrobian, M., 2006. Calculation of liquidus temperature for steel by Le Chatelier-Shreder and van Laar-Bowen equations. Kov. Mater. 44, 181–184.

Kozakevi.P, Olette, M., 1971. Role of Surface Phenomena in Mechanism Used for Eliminating Solid Inclusions. Rev. Metall. 68, 635–646.

Laforest, G., Duchesne, J., 2006. Characterization and leachability of electric arc furnace dust made from remelting of stainless steel. J. Hazard. Mater. 135, 156–164.

Lebukhova, N. V., Karpovich, N.F., 2008. Carbothermic reduction of copper, nickel, and cobalt oxides and molybdates. Inorg. Mater. 44, 890–893.

Lebukhova, N. V., Karpovich, N.F., 2006. Carbothermic reduction of cobalt and nickel tungstates. Inorg. Mater. 42, 310–315.

Lemperle, M., Rachner, H.-J., Fechner, R., Kasun, D., 2011. OxyCup furnace-Smelting steelmill fines, dust and sludge to liquid hot metal and slag. AISTech 149–160.

Lindblom, B., 2005. Mechanism study on solid-state reduction in the Fe 2 O 3 – NiO – Cr 2 O 3 – C system using thermal analyses 22–30.

Liu, C., Huang, S., Wollants, P., Blanpain, B., Guo, M., 2017. Valorization of BOF Steel Slag by Reduction and Phase Modification: Metal Recovery and Slag Valorization. Metall. Mater. Trans. B 48, 1602–1612.

Long, H.M., Li, J.X., Wang, P., Shi, S.Q., 2012. Reduction kinetics of carbon containing pellets made from metallurgical dust. Ironmak. Steelmak. 39, 585–592.

Lozano-Lunar, A., Raposeiro da Silva, P., de Brito, J., Fernández, J.M., Jiménez, J.R., 2019. Safe use of electric arc furnace dust as secondary raw material in self-compacting mortars production. J. Clean. Prod. 211, 1375–1388.

Ma, G., Garbers-Craig, A.M., 2006. Cr(VI) containing electric furnace dusts and filter cake from a stainless steel waste treatment plant: Part 2 - Formation mechanisms and leachability. Ironmak. Steelmak. 33, 238–244.

Martín, M.I., López, F.A., Rabanal, M.E., Torralba, J.M., 2010. Production of sponge iron powder by reduction of a by-product of the steelmaking industry. Proc. World Powder Metall. Congr. Exhib. World PM 2010 1, 1–6.

Martín, M.I., López, F.A., Torralba, J.M., 2012. Production of sponge iron powder by reduction of rolling

mill scale. Ironmak. Steelmak. 39, 155–162.

Mikli, V., Kaerdi, H., Kulu, P., Besterci, M., 2001. Characterization of powder particle morphology. Proc. Est. Acad. Sci. Eng. 7, 22–34.

Mymrin, V., Nagalli, A., Catai, R.E., Izzo, R.L.S., Rose, J., Romano, C.A., 2016. Structure formation processes of composites on the base of hazardous electric arc furnace dust for production of environmentally clean ceramics. J. Clean. Prod. 137, 888–894.

Nakayama, M., 2012. EAF dust treatment for high metal recovery. SEAISI Quarterly(South East Asia Iron Steel Institute) 41, 22–26.

Nogi, K., Ogino, K., 1983. Role of Interfacial Phenomena in Deoxidation Process of Molten Iron. Can. Metall. Q. 22, 19–28.

Pereira, C.F., Galiano, Y.L., Rodríguez-Piñero, M.A., Parapar, J.V., 2007. Long and short-term performance of a stabilized/solidified electric arc furnace dust. J. Hazard. Mater. 148, 701–707.

Perry, D.L., 2011. Handbook of inorganic compounds, 2nd ed. ed. CRC Press, New York.

Ramakrishnan, P., 1983. Iron powder from iron scrap. Conserv. Recycl. 6, 49–54.

Ri, S., Chu, M., 2015. Separation of metal nugget from self-reduced product of coal composite stainless steel dust briquette. ISIJ Int. 55, 1565–1572.

Ri, S.C., Chu, M.S., Chen, S.Y., Liu, Z.G., Hong, H., 2016. Self-reduction Mechanism of Coal Composite Stainless Steel Dust Hot Briquette. J. Iron Steel Res. Int. 23, 314–321.

Sayadi, M., Hesami, S., 2017. Performance evaluation of using electric arc furnace dust in asphalt binder. J. Clean. Prod. 143, 1260–1267.

Sofilić, T., Rastovčan-Mioč, A., Cerjan-Stefanović, Š., Novosel-Radović, V., Jenko, M., 2004. Characterization of steel mill electric-arc furnace dust. J. Hazard. Mater. 109, 59–70.

Suzuki, R.O., Tatemoto, K., Kitagawa, H., 2004. Direct synthesis of the hydrogen storage V–Ti alloy powder from the oxides by calcium co-reduction. J. Alloys Compd. 385, 173–180.

Takano, C., Cavallante, F.L., Martins Dos Santos, D., Mourão, M.B., 2005. Recovery of Cr, Ni and Fe from dust generated in stainless steelmaking. Trans. Institutions Min. Metall. Sect. C Miner. Process. Extr. Metall. 114.

Tang, Z., Ding, X., Yan, X., Dong, Y., Liu, C., 2018. Recovery of iron, chromium, and nickel from pickling sludge using smelting reduction. Metals (Basel).

Tsuji, H., 2012. Behavior of reduction and growth of metal in smelting of saprolite Ni-ore in a rotary kiln

for production of ferro-nickel alloy. ISIJ Int. 52, 1000–1009.

Voorhees, P.W., 1985. The theory of Ostwald ripening. J. Stat. Phys. 38, 231–252.

Walther, G., Böttner, T., Kieback, B., Weißgärber, T., Hoffmann, M., 2015. New processing route for production of fine spherical iron powder. Proc. Euro PM 2015 Int. Power Metall. Congr. Exhib. 1–6.

Wu, P., Eriksson, G., Pelton, A.D., 1993. Critical evaluation and optimization of the thermodynamic properties and phase diagrams of the CaO–FeO, CaO–MgO, CaO–MnO, FeO–MgO, FeO–MnO, and MgO–MnO systems. J. Am. Ceram. Soc. 76, 2065–2075.

Wu, X., Xing, J., Fu, H., Zhi, X., 2007. Effect of titanium on the morphology of primary M7C3 carbides in hypereutectic high chromium white iron. Mater. Sci. Eng. A 457, 180–185.

Xia, L. ge, Mao, R., Zhang, J. liang, Xu, X. nan, Wei, M. fang, Yang, F. hua, 2015. Reduction process and zinc removal from composite briquettes composed of dust and sludge from a steel enterprise. Int. J. Miner. Metall. Mater. 22, 122–131.

Yang, C. cong, Pan, J., Zhu, D. qing, Guo, Z. qi, Li, X. ming, 2019. Pyrometallurgical recycling of stainless steel pickling sludge: a review. J. Iron Steel Res. Int. 26, 547–557.

Ye, G., Burström, E., Kuhn, M., Piret, J., 2003. Reduction of steel-making slags for recovery of valuable metals and oxide materials. Scand. J. Metall. 32, 7–14.

Yolton, C.F., Froes, F.H.S., 2015. Conventional titanium powder production, in: Titanium Powder Metallurgy. Elsevier, pp. 21–32.

Yoshikawa, N., Mashiko, K.I., Sasaki, Y., Taniguchi, S., Todoroki, H., 2008. Microwave carbo-thermal reduction for recycling of Cr from Cr-containing steel making wastes. ISIJ Int. 48, 690–695.

Zhang, H.N., Li, J.L., Xu, A. jun, Yang, Q.X., He, D.F., Tian, N.Y., 2014. Carbothermic reduction of zinc and iron oxides in electric arc furnace dust. J. Iron Steel Res. Int. 21, 427–432.

Zhang, Y., Shibata, E., Kasai, E., Nakamura, T., 2006. Vapor pressure of zinc and zinc chloride in the FetO-CaO-SiO2-Al2O3 slag system. Mater. Trans. 47, 1341–1346.